



Thermal annealing study of the mid-infrared aluminum nitride on insulator (AINOI) photonics platform

BOWEI DONG,^{1,2,3,4} XIANSHU LUO,⁵ SHIYANG ZHU,² TING HU,² MO LI,^{6,7} DIHAN HASAN,^{1,3} LI ZHANG,⁸ SOO JIN CHUA,⁸ JINGXUAN WEI,^{1,3} YUHUA CHANG,^{1,3} YIMING MA,^{1,3} PHILIPPE VACHON,^{1,3} GUO-QIANG LO,⁵ KAH WEE ANG,^{1,3} DIM-LEE KWONG,² AND CHENGKUO LEE^{1,2,3,*}

¹Department of Electrical and Computer Engineering, National University of Singapore, Singapore 117576, Singapore

²Institute of Microelectronics, Agency for Science, Technology and Research (A*STAR), Singapore 138634, Singapore

³Center for Intelligent Sensors and MEMS (CISM), National University of Singapore, Singapore 117576, Singapore

⁴NUS Graduate School for Integrative Sciences and Engineering, National University of Singapore, Singapore 119077, Singapore

⁵Advanced Micro Foundry, Pte. Ltd., 11 Science Park Road, Singapore Science Park II, Singapore 117685, Singapore

⁶Department of Electrical and Computer Engineering, University of Washington, Seattle, WA 98195, USA

⁷Department of Physics, University of Washington, Seattle, WA 98195, USA

⁸Low Energy Electronic Systems, Singapore-MIT Alliance for Research and Technology, Singapore 138602, Singapore

*elelc@nus.edu.sg

Abstract: Aluminum nitride on insulator (AINOI) photonics platform has great potential for mid-infrared applications thanks to the large transparency window, piezoelectric property, and second-order nonlinearity of AlN. However, the deployment of AINOI platform might be hindered by the high propagation loss. We perform thermal annealing study and demonstrate significant loss improvement in the mid-infrared AINOI photonics platform. After thermal annealing at 400°C for 2 hours in ambient gas environment, the propagation loss is reduced by half. Bend loss and taper coupling loss are also investigated. The performance of multimode interferometer, directional coupler, and add/drop filter are improved in terms of insertion loss, quality factor, and extinction ratio. Fourier-transform infrared spectroscopy, Raman spectroscopy, and X-ray diffraction spectroscopy suggest the loss improvement is mainly attributed to the reduction of extinction coefficient in the silicon dioxide cladding. Apart from loss improvement, appropriate thermal annealing also helps in reducing thin film stress.

© 2019 Optical Society of America under the terms of the [OSA Open Access Publishing Agreement](#)

1. Introduction

The deployment of intelligent robotics and Internet of things (IoT) demands complex sensor networks which consist of numerous sensor nodes. Mid-infrared (MIR) is an ideal wavelength range in the electromagnetic (EM) wave spectrum for sensing applications. MIR contains two atmospheric transmission windows (3-5 μm and 8-14 μm) which serve as the platform for remote sensing [1,2]. More significantly, MIR covers the vibrational molecular fingerprints of many organic matters and biological agents in the gaseous or liquid form [3,4]. Label-free sensing are envisaged in MIR sensing due to the strong light-matter interaction at characteristic wavelength of individual molecules [5,6]. MIR sensing is thus a prominent

solution for environmental monitoring and healthcare monitoring. To date, glucose detection [7], monolayer protein detection [8], genome detection [9], exhaled breath monitoring [10], methane sensing [11], heavy water sensing [12], greenhouse gases sensing [13] and volatile organic compounds sensing [14] have been demonstrated by MIR spectroscopy.

Besides its promising sensing capability, the value of MIR sensing lies in its fabrication compatibility with the matured complementary metal-oxide-semiconductor (CMOS) fabrication technology. Planar MIR devices (or MIR waveguide devices) can leverage CMOS fabrication technologies to achieve low-cost and high-performance devices. There are research efforts investigating several CMOS-compatible material platforms to develop a complete library for MIR, including silicon-on-insulator [15,16], silicon-on-sapphire [17], silicon nitride-on-insulator [18,19], germanium-on-insulator [20,21], germanium-on-silicon [22,23], germanium-on-silicon nitride [24], and silicon-germanium alloy-on-silicon [25,26]. Wet-etch technique is also employed to undercut the insulation layer to achieve suspended waveguide-on-air structure, preventing absorption from insulation layer [27–29]. Chalcogenide glass, although not CMOS-compatible, is also gaining more attentions due to its wide MIR transparency window and the potential for on-chip integration [30,31].

Recently, the aluminum nitride on insulator (AlNOI) platform for MIR photonics has been reported [32]. AlN offers advantages such as CMOS-compatibility, wide transparency window (0.2 – 13.6 μm) [33] and high resistance to chemical and thermal perturbation [34]. The AlNOI platform can potentially offer piezoelectric tuning capability [35] and optical nonlinearity [36] enabled by its atomic structural asymmetry in the *c*-axis. Despite most of the good optical performances achieved in the reported AlNOI MIR photonics platform, one major drawback is the high propagation loss.

In this paper, we study the thermal annealing effect on the MIR AlNOI photonics platform and demonstrate significant loss improvement. In the wavelength range from 3.66 to 3.90 μm , using the optimal thermal annealing condition of 400°C for 2 hours (hrs) in ambient gas environment, the propagation loss is reduced to half at 0.8 dB/mm. The cascaded multimode interferometer (MMI) shows lower insertion loss, while the add/drop filter presents higher quality (Q) factor accompanied by larger extinction ratio (ER). An effective index change is also suggested by the characterization of directional coupler (DC) and add/drop filter. Fourier-transform infrared (FTIR) spectroscopy, Raman spectroscopy, and X-ray diffraction (XRD) are employed to study the loss improvement and stress effect in thermal annealing. This work shows the first step towards performance enhancement in MIR AlNOI photonics platform that has potential for broadband operation and three-dimensional integration for microelectromechanical systems (MEMS)-based photonics.

2. Device characterization

The device fabrication starts from a commercially available 8 in silicon (Si) wafer. A 3 μm silicon dioxide (SiO_2) bottom cladding is deposited by plasma enhanced chemical vapor deposition (PECVD) with silane (SiH_4) precursor, followed by chemical-mechanical planarization (CMP) to provide a flat and smooth surface for AlN deposition. Then 1.2 μm AlN thin film is deposited by reaction DC magnetron sputtering. SiO_2 is deposited as hard mask for waveguide pattern definition. After etching the SiO_2 hard mask, the pattern is transferred to the AlN layer using deep ultraviolet lithography (DUV) and deep reactive ion etching (DRIE). A deep trench more than 100 μm for fiber butt coupling is formed after a 3 μm SiO_2 thin film is deposited as the upper cladding. The 8 in wafer with completed AlN waveguide patterns then undertakes the thermal annealing process. Seven annealing conditions are examined. The details of annealing conditions are shown in Table.1. The 8 in wafer is finally diced for characterization. The characterization setup is described in our previous work [37].

Table 1. Examined thermal annealing conditions

Wafer number	1	2	3	4	5	6	7
Temperature (°C)	400	400	400	600	800	1000	1000
Duration (hours)	2	6	12	4	4	2	6
Gas environment	Ambient	Ambient	Ambient	Ambient	Ambient	Ambient	Ambient
Crevice	No	No	No	No	Slight	Moderate	Severe

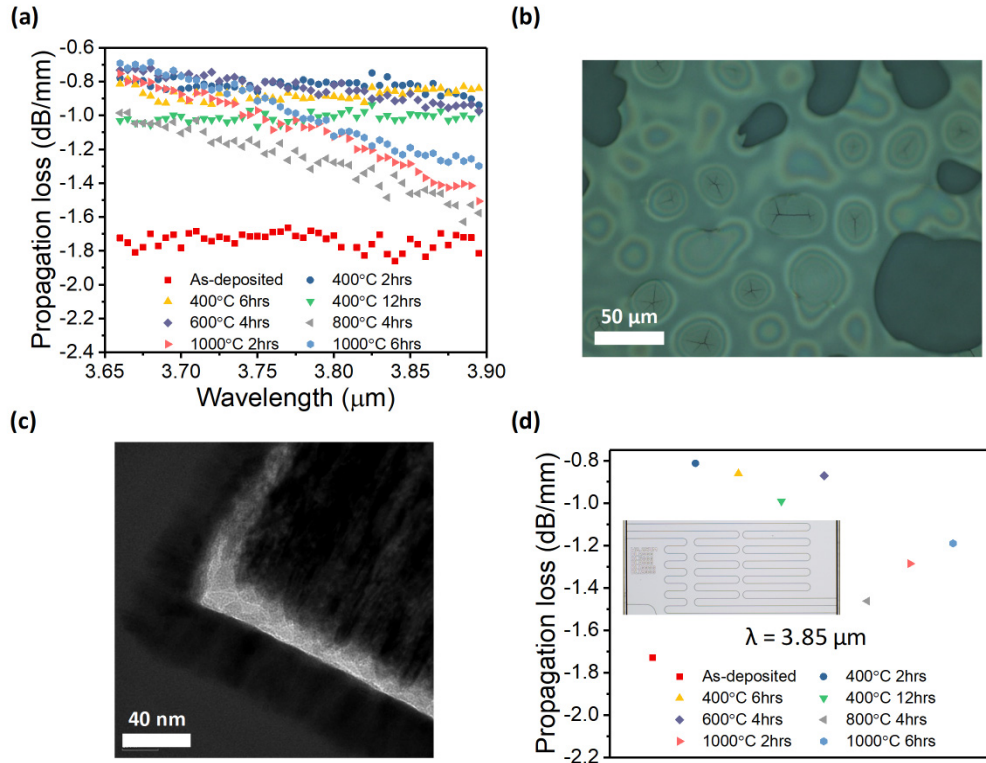


Fig. 1. Waveguide propagation loss after thermal annealing under different conditions. (a) Wavelength dependent loss. (b) Optical microscope image showing crevices on the thin film after the device undergoes thermal annealing at 800°C for 4 hrs. (c) Tunneling electron microscope (TEM) image of the waveguide cross section showing crevices around the waveguide sidewalls after the device undergoes thermal annealing at 800°C for 4 hrs. (d) Loss at 3.85 μm . Inset: Waveguide structure for extracting propagation loss using cutback method.

The waveguide cross section has the dimension of $H1.2 \mu\text{m} \times W2.25 \mu\text{m}$ to ensure single mode condition while allowing significant evanescent field for coupling. Figure 1(a) shows the propagation loss of AlN waveguide after thermal annealing under different conditions. Without thermal annealing, the as-deposited waveguide shows an average propagation loss of 1.74 dB/mm across the wavelength range. After thermal annealing at 400°C for 2 hours, the propagation loss is effectively reduced to 0.82 dB/mm. Thermal annealing at 400°C or 600°C results in stable propagation loss across the wavelength range. On contrary, after thermal annealing at 800°C or 1000°C, the propagation loss increases almost linearly with respect to the wavelength. The rates of increase are similar. This could be attributed to the higher scattering loss caused by the formation of crevices around the waveguide sidewalls (Fig. 1(b)).

and 1(c)). An analytical formula to calculate sidewall roughness induced scattering loss was proposed by Payne and Lacey [38]:

$$\alpha_{\max} = \frac{\lambda \sigma^2 K}{2\pi d^4 n_1}, \quad (1)$$

where α_{\max} is the upper bound of scattering loss, σ is the root-mean square surface roughness, K is a coefficient depending on waveguide geometry and the statistical distribution of surface roughness, λ is the wavelength in vacuum, d is half of the waveguide width, and n_1 is the effective index of propagating light. As crevices are formed, σ increases so that scattering loss can be dominant. α_{\max} is proportional to λ so that longer wavelength experiences higher loss. As shown in Fig. 1(a), the linear relationship between the propagation loss and λ also agrees with this analytical formula.

As shown in Fig. 1(d), at 3.85 μm , a 400°C or a 600°C thermal annealing improves the propagation loss while a thermal annealing higher than 800°C introduces additional loss. Since thermal annealing at 400°C for 2 hrs achieves the lowest propagation loss without wafer crevices, the following characterization focuses on the devices annealed by this specific thermal annealing condition.

Figure 2 presents the comparison of bend loss and taper coupling loss before and after thermal annealing. Figure 2(a) shows that bends with radius $R = 25 \mu\text{m}$ and $R = 50 \mu\text{m}$ exhibit bend loss inferior to 0.2 dB/90° before thermal annealing. $R = 75 \mu\text{m}$ bend presents a higher loss at 0.27 dB/90°, indicating that absorption loss and scattering loss are dominant. After thermal annealing, the loss of $R = 75 \mu\text{m}$ bend is reduced to 0.2 dB/90°. However, $R = 25 \mu\text{m}$ bend experiences higher loss. The rise of bend loss in $R = 25 \mu\text{m}$ bend is attributed to the higher scattering loss. As light propagates through smaller bends, there is larger overlap between the mode and the waveguide sidewall so that it is more vulnerable to scattering caused by the increase sidewall roughness after thermal annealing. $R = 50 \mu\text{m}$ and $R = 75 \mu\text{m}$ bend experience less additional scattering loss because the overlap between the mode and the waveguide sidewall is smaller.

The taper coupling loss of both forward taper and inverse taper before and after thermal annealing are shown in Fig. 2(c) and 2(d). Since the waveguide width is 2.25 μm , 1 μm and 2 μm tapers are inverse tapers while the rests are all forward taper. The taper coupling efficiency does not benefit from the thermal annealing treatment as the coupling loss scatters between -10 dB/facet to -14 dB/facet both before and after thermal annealing. Therefore, wider forward taper and narrower inverse taper are desired to improve the taper coupling efficiency. It is worth noting there is a current constraint on the inverse taper. As shown in the inset of Fig. 2(c), the 1 μm inverse taper shows smooth and clear profile while the 0.3 μm inverse taper is not successfully fabricated. The fabrication process should be further improved to achieve narrower inverse taper.

The characterizations of passive functional devices including cascaded MMI, DC, and add/drop filter before and after thermal annealing are shown in Fig. 3. The optical images of the tested devices are presented in the right most column. Comparing Fig. 3(a) and 3(d), the average slopes of transmission from cascaded ports in MMI are -3.99 dB \pm 0.21 dB and -3.49 dB \pm 0.07 dB before and after thermal annealing respectively. The average and standard deviation are calculated with respect to different wavelengths, namely 3.7 μm , 3.75 μm , 3.8 μm , and 3.85 μm . Apart from the insertion loss improvement from -0.99 dB to -0.49 dB, thermal annealing also helps in reducing standard deviation across different wavelengths, enhancing broadband operation capability. Figure 3(b) and 3(e) presents the performance of DC at 3.7 μm . It is worthy to note that the coupling length for 100% power transfer L_π in DC varies from 46.7 μm before thermal annealing to 44.2 μm after thermal annealing. According to the equation of ideal DC:

$$L_{\pi} = (\lambda / 2) \times (n_{eff1} - n_{eff2}), \quad (2)$$

where λ is the working wavelength and n_{eff1} and n_{eff2} are the effective index of the symmetric and asymmetric mode in the DC, the drop of L_{π} reveals the decrease in $(n_{eff1} - n_{eff2})$, suggesting a drop of refractive index in the material. The comparison of add/drop filter's performances before and after thermal annealing is shown in Fig. 3(c) and 3(f). The add/drop filter has a ring radius of 50 μm and coupling gap of 0.6 μm . The solid lines in both Figs show the Lorentzian fit of the resonance peak. After thermal annealing, the Q factors at the drop port and through port both increase from 2000 to 3000, suggesting a higher ratio of the stored energy to the power loss thanks to the loss improvement. The ER at the through port also drastically rises from 7 dB to 15 dB. The resonance peak originally located at 3.681 μm shifts to 3.668 μm after thermal annealing, suggesting a decrease in material refractive index. This result agrees with DC characterization result.

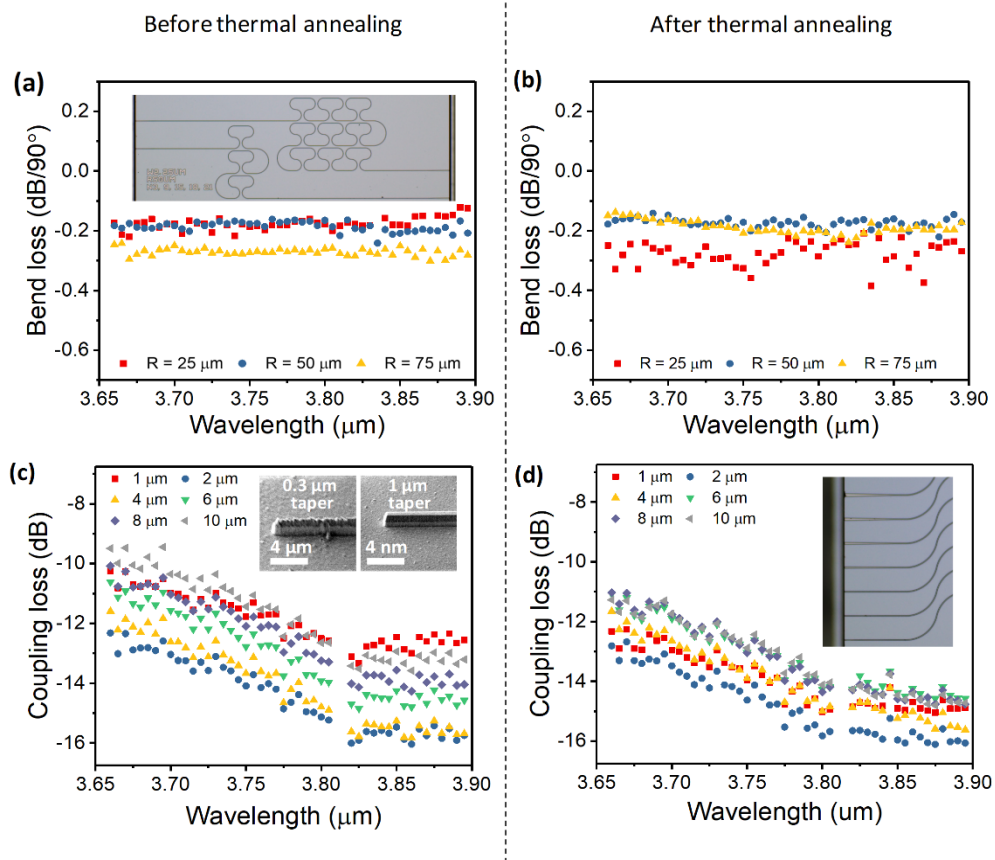


Fig. 2. The comparison of bend loss and taper coupling efficiency before and after thermal annealing. (a) Bend loss before thermal annealing. Inset: Optical image of waveguide structure for extracting bend loss using cutback method. (b) Bend loss after thermal annealing. (c) Taper coupling loss before thermal annealing. Inset: SEM images of 0.3 μm and 1 μm inverse tapers. (d) Taper coupling loss after thermal annealing. Inset: Optical image of tapers with different widths.

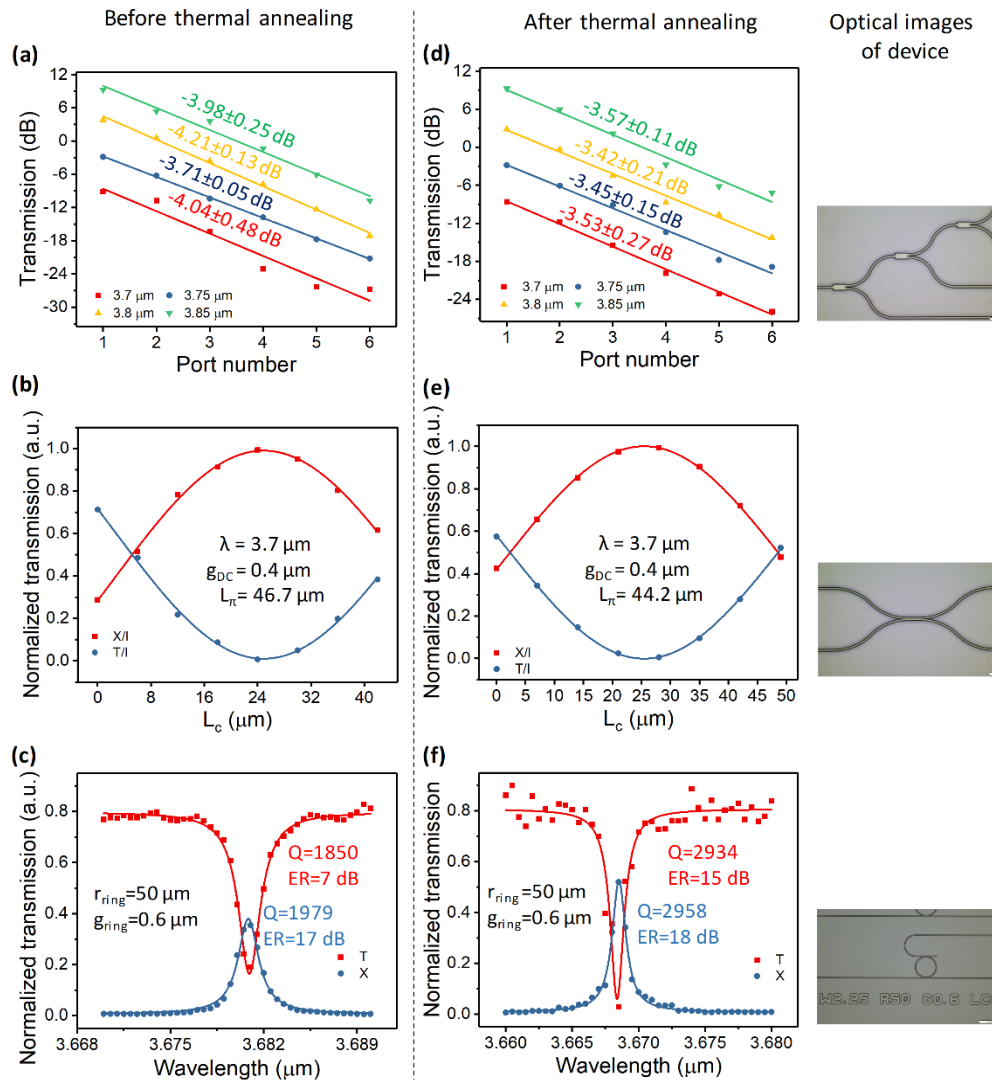


Fig. 3. The comparison of performance of three functional building blocks before and after thermal annealing. (a) Cascaded MMI. (b) DC. (c) Add/drop filter. before thermal annealing. (d) Cascaded MMI. (e) DC. (f) Add/drop filter. after thermal annealing.

3. Analysis and discussion

FTIR, Raman, and XRD spectroscopy are employed to analyze the loss improvement and stress effect in thermal annealing. Figure 4 shows the FTIR characterization result. In AlN-on-SiO₂ wafer (Fig. 4(a)), several interference peaks in the transmittance spectrum are caused by thin-film interference where reflections happen at the air/AlN interface and AlN/SiO₂ interface. 1000°C 2hrs and 1000°C 6hrs curves show different patterns due to wafer crevices. Despite undertaking thermal annealing under different conditions, the constructed interference peak at 3.77 μm remains at the same wavelength. However, as shown in Fig. 4(b), in SiO₂-on-Si wafer the constructive interference peak at 3.61 μm shifts to shorter wavelength after thermal annealing. The exact interference peaks from both wafers after thermal annealing are plotted in Fig. 4(c). It is obvious that blue-shift happens in SiO₂-on-Si but not in AlN-on-SiO₂ wafer. According to the constructive interference condition:

$$2nd \cos \theta = m\lambda, \quad (3)$$

where n is the material refractive index, d is the thin film thickness; assuming normal incidence and constant thin film thickness, the blue-shift of constructive interference peak in SiO₂-on-Si wafer indicates the decrease of SiO₂'s refractive index. This is also in agreement with the L_{π} drop when comparing Fig. 3(b) and 3(e), and the decrease of resonance wavelength when comparing Fig. 3(c) and 3(f). Moreover, the FTIR characterization results exhibit whole spectrum shift in SiO₂-on-Si wafer, but not in AlN-on-SiO₂ wafer, indicating that the refractive index drops across the wavelength range in SiO₂ and remains relatively constant in AlN. The Kramer-Kronig relation states:

$$n(\omega') = 1 + \frac{2}{\pi} P \int_0^{\infty} \frac{\omega k(\omega)}{\omega^2 - \omega'^2} d\omega, \quad (4.1)$$

$$k(\omega') = -\frac{2\omega'}{\pi} P \int_0^{\infty} \frac{n(\omega) - 1}{\omega^2 - \omega'^2} d\omega, \quad (4.2)$$

where n and k are the refractive index and extinction coefficient respectively; P is the Cauchy principle value; ω' is the EM wave angular frequency. According to Eq. (4.2), since $n(\omega)_{\text{SiO}_2}$ changes and $n(\omega)_{\text{AlN}}$ remains constant, it implies that after thermal annealing SiO₂ also experiences a change in its extinction coefficient $k(\omega)_{\text{SiO}_2}$ while the extinction coefficient of AlN $k(\omega)_{\text{AlN}}$ remains constant. Therefore, the loss improvement by thermal annealing can be mainly attributed to the drop of extinction coefficient in SiO₂.

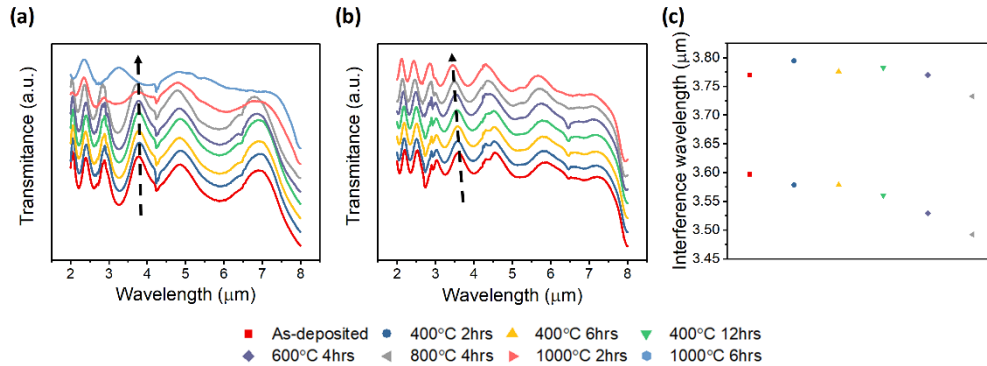


Fig. 4. FTIR spectrum before and after thermal annealing. (a) AlN-on-SiO₂. (b) SiO₂-on-Si. (c) the constructive interference peaks at around 3.7 μm originated from both thin films after thermal annealing under different conditions.

The Raman spectrum of the AlNOI wafer is presented in Fig. 5(a). All the major peaks are observed after thermal annealing under different conditions. The zoom-in to the E₂(high) peaks is shown in Fig. 5(b). The peaks are fitted with Lorentzian function. Within 800°C, as the thermal budget increases, the Raman peak shifts to higher wavenumbers, indicating that the compressive stress is building up in the thin film [39]. An abrupt decrease in wavenumber of the Raman peak after annealing at 1000°C suggests the release of compressive stress in the thin film. This could be attributed to the wafer crevices, as observed.

Figure 5(c) shows the XRD spectrum of the AlNOI wafer after thermal annealing under different conditions. Only single XRD peak at 36.04° is observed in all occasions, showing that the AlN thin films are highly c-axis (002) oriented after thermal annealing. The inset shows the full width at half-maximum (FWHM) of 0.16°, indicating the supreme piezoelectric property of the AlN thin film which comes close to the epitaxially grown AlN

[40]. Figure 5(d) zooms in to 36.04° in order to analyze the relative intensity change and XRD peak broadening. The peak shifts slightly to lower 2θ , accompanied by peak broadening. Such peak shift shows that compressive stress builds up upon thermal annealing [34], while the peak broadening indicates the existence of nonuniform micro strains. As shown in the inset of Fig. 5(d), the XRD intensity is very low in the as-deposited AlN thin film. It rises drastically upon thermal annealing; and starts to decrease at high thermal annealing temperature. With reference to [41], the stress in the thin film is negatively related to the XRD intensity. Hence, our XRD results indicate stress reduction in AlN thin film by thermal annealing at 400°C and 600°C . However, thermal annealing at higher temperature will introduce additional stress.

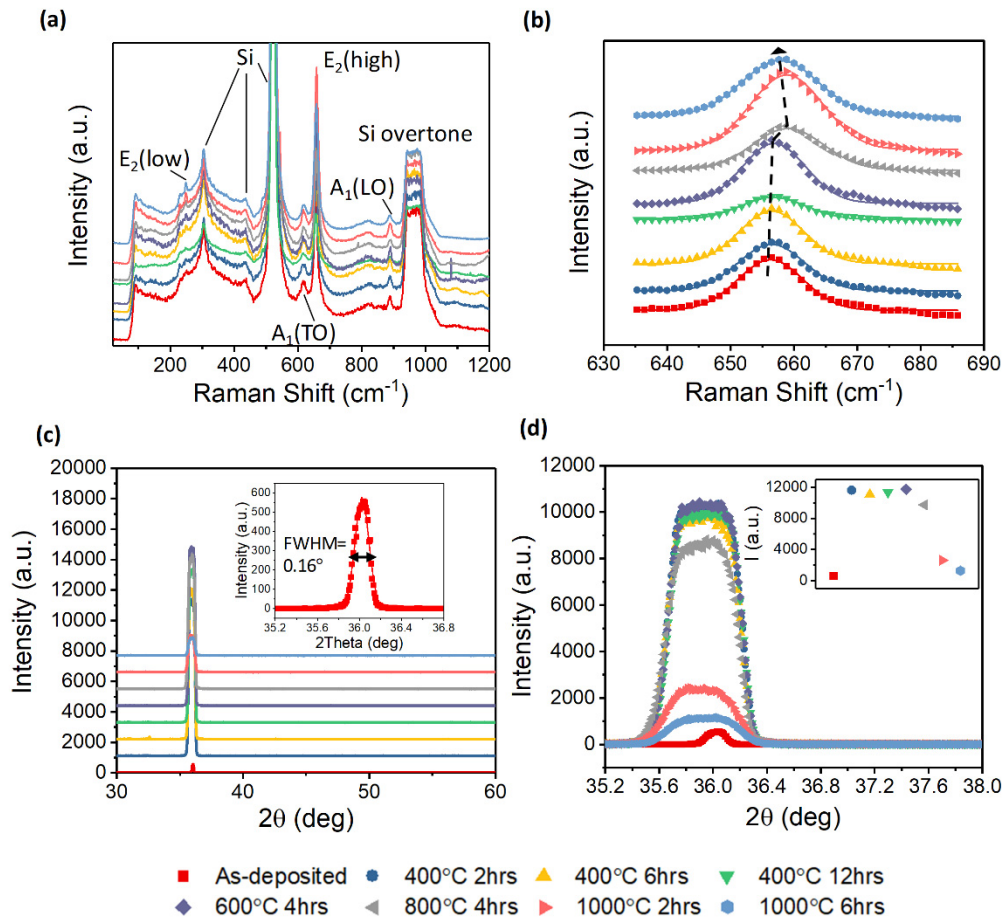


Fig. 5. (a) Raman spectrum of the AlNOI wafer after thermal annealing under different conditions. (b) Zoom-in of (a) to $E_2(\text{high})$ peaks. (c) XRD spectrum of the AlNOI wafer after thermal annealing under different conditions. Inset: Zoom-in of the XRD peak to $2\theta = 36^\circ$ in the as-deposited AlN thin film. (d) Zoom-in of (c) to $2\theta = 36^\circ$ with relative XRD intensity indicated. Inset: Values of XRD intensity after thermal annealing under different conditions.

Moreover, the Raman and XRD spectrum also help eliminating the occurrence of partial Al atoms in Al-rich AlN film becoming AlO, which is also possibly the cause for the blue shift of resonance peak in add/drop filters. According to [42], the formation of $\gamma\text{-Al}_2\text{O}_3$ and $\alpha\text{-Al}_2\text{O}_3$ will introduce several diffraction peaks in the XRD spectrum. Two Raman peaks located at 383 cm^{-1} and 421 cm^{-1} should also be observed. However, in our Raman and XRD spectroscopy characterization results (See Fig. 5(a) and 5(c)), 383 cm^{-1} and 421 cm^{-1} peaks

are not presented in the Raman spectrum while only a single peak at 36° is observed in the XRD spectrum. Hence, we believe the refractive index change is not induced by partial Al atoms in Al-rich AlN film becoming AlO.

After thermal annealing at 400°C for 2hrs in ambient gas environment, the MIR AlNOI photonics platform possesses reduced loss and lower wafer stress. It brings many benefits. Firstly, the thermal annealing condition is compatible with the temperature requirement in CMOS fabrication process. Thus, the whole fabrication of AlNOI portion could be easily suited to the existing fabrication processes. It is possible to fabricate AlN photonics layer on top, after the completion of Si photonics layer, providing a method to realize three-dimensional integration to achieve more compact devices [43]. Secondly, the AlN device layer can be shallowly etched followed by buried SiO_2 undercut with releasing holes. MEMS cantilever can be designed to hold and tune the suspended waveguide [44], while surface acoustic wave can be introduced for high frequency modulation [45]. Thirdly, by utilizing the second-order nonlinearity of AlN, high frequency modulation can be achieved by supplying alternating electric field penetrating through the AlN waveguide [46]. It can be a solution for on-chip high frequency modulation in the MIR where Si modulation experiences high loss due to the abrupt increase in the extinction coefficient of SiO_2 caused by the free-carrier dispersion effect in the MIR [47,48]. However, the thickness of the AlN thin film in our MIR AlNOI photonics platform is as thick as $1.2\ \mu\text{m}$ to ensure tight mode confinement and compact devices. Considering the fabrication limitation that produces a side wall slope of around 75° to 80° , it is not easy to fabricate device with small feature size such as subwavelength structures [49,50] and photonic crystals [51–54]. One solution could be enabling these device functions in the bottom Si photonics layers. Light can thereafter be transferred to the AlN layer for other operations [55]. Another solution could involve the integration of photonics and plasmonics where short plasmonic features can perform the desired optical functions while breaking the optical diffraction limit [56–58]. In order to further reduce the loss of the MIR AlNOI platform, we are investigating replacing silane based PECVD SiO_2 by TEOS SiO_2 or thermal SiO_2 for better cladding quality, and optimizing the etching process to achieve better sidewall smoothness and smaller slope.

4. Conclusion

We report loss improvement in the MIR AlNOI photonics platform by studying the thermal annealing effect. Wafer crevices are observed after thermal annealing beyond 800°C . After the optimal thermal annealing condition of 400°C for 2 hours in ambient gas environment, the average waveguide propagation loss in 3.66 to $3.9\ \mu\text{m}$ reduces by half from $1.74\ \text{dB/mm}$ to $0.82\ \text{dB/mm}$. The insertion loss is reduced in cascaded MMI while higher Q factor around 3000 and larger ER around 15 dB are achieved in add/drop filter. The performance of DC and add/drop filter together with FTIR characterization results suggest the loss improvement could be attributed to the reduction of the extinction coefficient in SiO_2 cladding. The Raman and XRD spectroscopy results indicate that proper annealing also helps in releasing thin film stress. This work presents the optimization of MIR AlNOI photonics platform in terms of loss reduction and performance improvement of the passive functional building blocks. The low-loss MIR AlNOI photonics platform could have better synergy with other established MIR photonics platform through three-dimensional integration. Leveraging the wide transparency window for broadband operation, piezoelectric property for accurate tuning, and second-order nonlinearity for high speed electro-optic modulation, the advancement in AlNOI photonics platform will pave the way for MEMS-based photonics and novel applications in MIR sensing.

Funding

National Research Foundation Singapore; Research Grant of CRP-15th (NRF-CRP15-2015-02) “Piezoelectric Photonics Using CMOS Compatible AlN Technology for Enabling the

Next Generation Photonics ICs and Nanosensors” at the National University of Singapore, the NRF-ISF (NRF2015-NRF-ISF001-2620 NUS) “Reconfigurable data center optical interconnects using fast nanophotonic MEMS waveguide switches”.

References

1. Y. Zou, S. Chakravarty, C.-J. Chung, X. Xu, and R. T. Chen, “Mid-infrared silicon photonic waveguides and devices [Invited],” *Photon. Res.* **6**(4), 254–276 (2018).
2. H. Lin, Z. Luo, T. Gu, L. C. Kimerling, K. Wada, A. Agarwal, and J. Hu, “Mid-infrared integrated photonics on silicon: A perspective,” *Nanophotonics* **7**(2), 393–420 (2017).
3. T. Hu, B. Dong, X. Luo, T.-Y. Liow, J. Song, C. Lee, and G.-Q. Lo, “Silicon photonic platforms for mid-infrared applications [Invited],” *Photon. Res.* **5**(5), 417–430 (2017).
4. B. Mizaikoff, “Waveguide-enhanced mid-infrared chem/bio sensors,” *Chem. Soc. Rev.* **42**(22), 8683–8699 (2013).
5. P. T. Lin, H. G. Lin, Z. Han, T. Jin, R. Millender, L. C. Kimerling, and A. Agarwal, “Label-free glucose sensing using chip-scale mid-infrared integrated photonics,” *Adv. Opt. Mater.* **4**(11), 1755–1759 (2016).
6. P. T. Lin, S. W. Kwok, H. Y. G. Lin, V. Singh, L. C. Kimerling, G. M. Whitesides, and A. Agarwal, “Mid-infrared spectrometer using opto-nanofluidic slot-waveguide for label-free on-chip chemical sensing,” *Nano Lett.* **14**(1), 231–238 (2014).
7. E. Ryckeboer, R. Bockstaele, M. Vanslembrouck, and R. Baets, “Glucose sensing by waveguide-based absorption spectroscopy on a silicon chip,” *Biomed. Opt. Express* **5**(5), 1636–1648 (2014).
8. D. Rodrigo, O. Limaj, D. Janner, D. Etezadi, F. J. García De Abajo, V. Pruneri, and H. Altug, “Mid-infrared plasmonic biosensing with graphene,” *Science* **349**(6244), 165–168 (2015).
9. A. A. Leonardi, M. J. Lo Faro, S. Petralia, B. Fazio, P. Musumeci, S. Conoci, A. Irrera, and F. Priolo, “Ultrasensitive label- and PCR-free genome detection based on cooperative hybridization of silicon nanowires optical biosensors,” *ACS Sens.* **3**(9), 1690–1697 (2018).
10. F. Seichter, A. Wilk, K. Wörle, S. S. Kim, J. A. Vogt, U. Wachter, P. Radermacher, and B. Mizaikoff, “Multivariate determination of $^{13}\text{CO}_2/^{12}\text{CO}_2$ ratios in exhaled mouse breath with mid-infrared hollow waveguide gas sensors,” *Anal. Bioanal. Chem.* **405**(14), 4945–4951 (2013).
11. L. Tombez, E. J. Zhang, J. S. Orcutt, S. Kamlapurkar, and W. M. J. Green, “Methane absorption spectroscopy on a silicon photonic chip,” *Optica* **4**(11), 1322–1325 (2017).
12. N. Singh, A. Casas-Bedoya, D. D. Hudson, A. Read, E. Mägi, and B. J. Eggleton, “Mid-IR absorption sensing of heavy water using a silicon-on-sapphire waveguide,” *Opt. Lett.* **41**(24), 5776–5779 (2016).
13. L. Dong, F. K. Tittel, C. Li, N. P. Sanchez, H. Wu, C. Zheng, Y. Yu, A. Sampaolo, and R. J. Griffin, “Compact TDLAS based sensor design using interband cascade lasers for mid-IR trace gas sensing,” *Opt. Express* **24**(6), A528–A535 (2016).
14. Y. Chen, H. Lin, J. Hu, and M. Li, “Heterogeneously integrated silicon photonics for the mid-infrared and spectroscopic sensing,” *ACS Nano* **8**(7), 6955–6961 (2014).
15. S. A. Miller, M. Yu, X. Ji, A. G. Griffith, J. Cardenas, A. L. Gaeta, and M. Lipson, “Low-loss silicon platform for broadband mid-infrared photonics,” *Optica* **4**(7), 707–712 (2017).
16. M. Nedeljkovic, A. Z. Khokhar, Y. Hu, X. Chen, J. S. Penades, S. Stankovic, M. H. Chong, D. J. Thomson, F. Y. Gardes, G. T. Reed, and G. Z. Mashanovich, “Silicon photonic devices and platforms for the mid-infrared,” *Opt. Mater. Express* **3**(9), 1205–1214 (2013).
17. Y. Zou, H. Subbaraman, S. Chakravarty, X. Xu, A. Hosseini, W. C. Lai, P. Wray, and R. T. Chen, “Grating-coupled silicon-on-sapphire integrated slot waveguides operating at mid-infrared wavelengths,” *Opt. Lett.* **39**(10), 3070–3073 (2014).
18. P. T. Lin, V. Singh, H. Y. G. Lin, T. Tiwald, L. C. Kimerling, and A. M. Agarwal, “Low-stress silicon nitride platform for mid-infrared broadband and monolithically integrated microphotonics,” *Adv. Opt. Mater.* **1**(10), 732–739 (2013).
19. P. Tai Lin, V. Singh, L. Kimerling, and A. Murthy Agarwal, “Planar silicon nitride mid-infrared devices,” *Appl. Phys. Lett.* **102**(25), 251121 (2013).
20. J. Kang, M. Takenaka, and S. Takagi, “Novel Ge waveguide platform on Ge-on-insulator wafer for mid-infrared photonic integrated circuits,” *Opt. Express* **24**(11), 11855–11864 (2016).
21. T.-H. Xiao, Z. Zhao, W. Zhou, C.-Y. Chang, S. Y. Set, M. Takenaka, H. K. Tsang, Z. Cheng, and K. Goda, “Mid-infrared high-Q germanium microring resonator,” *Opt. Lett.* **43**(12), 2885–2888 (2018).
22. C. Alonso-Ramos, M. Nedeljkovic, D. Benedikovic, J. S. Penades, C. G. Littlejohns, A. Z. Khokhar, D. Pérez-Galacho, L. Vivien, P. Cheben, and G. Z. Mashanovich, “Germanium-on-silicon mid-infrared grating couplers with low-reflectivity inverse taper excitation,” *Opt. Lett.* **41**(18), 4324–4327 (2016).
23. M. Nedeljkovic, J. S. Penades, V. Mittal, G. S. Murugan, A. Z. Khokhar, C. Littlejohns, L. G. Carpenter, C. B. E. Gawith, J. S. Wilkinson, and G. Z. Mashanovich, “Germanium-on-silicon waveguides operating at mid-infrared wavelengths up to 8.5 μm ,” *Opt. Express* **25**(22), 27431–27441 (2017).
24. W. Li, P. Anantha, S. Bao, K. H. Lee, X. Guo, T. Hu, L. Zhang, H. Wang, R. Soref, and C. S. Tan, “Germanium-on-silicon nitride waveguides for mid-infrared integrated photonics,” *Appl. Phys. Lett.* **109**(24), 241101 (2016).
25. J. M. Ramirez, Q. Liu, V. Vakarini, J. Frigerio, A. Ballabio, X. Le Roux, D. Bouville, L. Vivien, G. Isella, and D. Marris-Morini, “Graded SiGe waveguides with broadband low-loss propagation in the mid infrared,” *Opt.*

- Express **26**(2), 870–877 (2018).
26. Q. Liu, J. M. Ramirez, V. Vakarín, X. Le Roux, J. Frigerio, A. Ballabio, E. T. Simola, C. Alonso-Ramos, D. Benedikovic, D. Bouville, L. Vivien, G. Isella, and D. Marris-Morini, “On-chip Bragg grating waveguides and Fabry-Perot resonators for long-wave infrared operation up to 8.4 μm ,” *Opt. Express* **26**(26), 34366–34372 (2018).
 27. J. S. Penadés, A. Sánchez-Postigo, M. Nedeljkovic, A. Ortega-Moñux, J. G. Wangüemert-Pérez, Y. Xu, R. Halir, Z. Qu, A. Z. Khokhar, A. Osman, W. Cao, C. G. Littlejohns, P. Cheben, I. Molina-Fernández, and G. Z. Mashanovich, “Suspended silicon waveguides for long-wave infrared wavelengths,” *Opt. Lett.* **43**(4), 795–798 (2018).
 28. Z. Cheng, X. Chen, C. Y. Wong, K. Xu, and H. K. Tsang, “Mid-infrared suspended membrane waveguide and ring resonator on silicon-on-insulator,” *IEEE Photonics J.* **4**(5), 1510–1519 (2012).
 29. J. Kang, Z. Cheng, W. Zhou, T.-H. Xiao, K.-L. Gopalakrisna, M. Takenaka, H. K. Tsang, and K. Goda, “Focusing subwavelength grating coupler for mid-infrared suspended membrane germanium waveguides,” *Opt. Lett.* **42**(11), 2094–2097 (2017).
 30. V. Mittal, M. Nedeljkovic, D. J. Rowe, G. S. Murugan, and J. S. Wilkinson, “Chalcogenide glass waveguides with paper-based fluidics for mid-infrared absorption spectroscopy,” *Opt. Lett.* **43**(12), 2913–2916 (2018).
 31. P. Su, Z. Han, D. Kita, P. Becla, H. Lin, S. Deckoff-Jones, K. Richardson, L. C. Kimerling, J. Hu, and A. Agarwal, “Monolithic on-chip mid-IR methane gas sensor with waveguide-integrated detector,” *Appl. Phys. Lett.* **114**(5), 051103 (2019).
 32. B. Dong, X. Luo, S. Zhu, M. Li, D. Hasan, L. Zhang, S. J. Chua, J. Wei, Y. Chang, G.-Q. Lo, K. W. Ang, D.-L. Kwong, and C. Lee, “Aluminum nitride on insulator (AINOI) platform for mid-infrared photonics,” *Opt. Lett.* **44**(1), 73–76 (2019).
 33. W. H. P. Pernice, C. Xiong, and H. X. Tang, “High Q micro-ring resonators fabricated from polycrystalline aluminum nitride films for near infrared and visible photonics,” *Opt. Express* **20**(11), 12261–12269 (2012).
 34. M. Gillinger, M. Schneider, A. Bittner, P. Nicolay, and U. Schmid, “Impact of annealing temperature on the mechanical and electrical properties of sputtered aluminum nitride thin films,” *J. Appl. Phys.* **117**(6), 065303 (2015).
 35. M. Mahmoud, A. Mahmoud, L. Cai, M. Khan, T. Mukherjee, J. Bain, and G. Piazza, “Novel on chip rotation detection based on the acousto-optic effect in surface acoustic wave gyroscopes,” *Opt. Express* **26**(19), 25060–25075 (2018).
 36. X. Guo, C.-L. Zou, and H. X. Tang, “Second-harmonic generation in aluminum nitride microrings with 2500%/W conversion efficiency,” *Optica* **3**(10), 1126–1131 (2016).
 37. B. Dong, X. Luo, T. Hu, T. X. Guo, H. Wang, D. L. Kwong, P. G. Q. Lo, and C. Lee, “Compact low loss mid-infrared for arbitrary power splitting ratio enabled by rib waveguide dispersion engineering,” *IEEE J. Sel. Top. Quantum Electron.* **24**(4), 4500108 (2018).
 38. F. P. Payne and J. P. R. Lacey, “A theoretical analysis of scattering loss from planar optical waveguides,” *Opt. Quantum Electron.* **26**(10), 977–986 (1994).
 39. X. H. Ji, Q. Y. Zhang, Z. Y. Ling, and S. P. Lau, “Stress and its effect on optical properties of AlN nanorods,” *Appl. Phys. Lett.* **95**(23), 233105 (2009).
 40. R. S. Naik, J. J. Lutsky, R. Reif, C. G. Sodini, A. Becker, L. Fetter, H. Huggins, R. Miller, J. Pastalan, G. Rittenhouse, and Y. H. Wong, “Measurements of the bulk, C-axis electromechanical coupling constant as a function of AlN film quality,” *IEEE Trans. Ultrason. Ferroelectr. Freq. Control* **47**(1), 292–296 (2000).
 41. N. Matsunami, H. Kakiuchida, M. Sataka, and S. Okayasu, “XRD characterization of AlN thin films prepared by reactive RF-sputter deposition,” *Adv. Mater. Phys. Chem.* **03**(01), 101–107 (2013).
 42. J. Gangwar, B. K. Gupta, S. K. Tripathi, and A. K. Srivastava, “Phase dependent thermal and spectroscopic responses of Al₂O₃ nanostructures with different morphogenesis,” *Nanoscale* **7**(32), 13313–13344 (2015).
 43. S. Zhu and G. Lo, “Vertically-stacked multilayer photonics on bulk silicon toward three dimensional untegration,” *J. Light. Technolgy* **34**(2), 386–392 (2016).
 44. T. J. Seok, N. Quack, S. Han, R. S. Muller, and M. C. Wu, “Large-scale broadband digital silicon photonic switches with vertical adiabatic couplers,” *Optica* **3**(1), 64–70 (2016).
 45. S. Ghosh and G. Piazza, “Elasto-optic modulator integrated in high frequency piezoelectric MEMS resonator,” in *MEMS 2016 Shanghai* (2016), (January), pp. 9–12.
 46. S. Zhu and G.-Q. Lo, “Aluminum nitride electro-optic phase shifter for backend integration on silicon,” *Opt. Express* **24**(12), 12501–12506 (2016).
 47. M. Nedeljkovic, S. Stanković, C. J. Mitchell, A. Z. Khokhar, S. A. Reynolds, D. J. Thomson, F. Y. Gardes, C. G. Littlejohns, G. T. Reed, and G. Z. Mashanovich, “Mid-infrared thermo-optic modulators in Si,” *IEEE Photonics Technol. Lett.* **26**(13), 1352–1355 (2014).
 48. M. Nedeljkovic, C. G. Littlejohns, A. Z. Khokhar, M. Banakar, W. Cao, J. S. Penades, D. T. Tran, F. Y. Gardes, D. J. Thomson, G. T. Reed, H. Wang, and G. Z. Mashanovich, “Silicon-on-insulator free-carrier injection modulators for the mid-infrared,” *Opt. Lett.* **44**(4), 915–918 (2019).
 49. B. Dong, T. Hu, X. Luo, Y. Chang, X. Guo, H. Wang, D.-L. Kwong, G.-Q. Lo, and C. Lee, “Wavelength-flattened directional coupler based mid-infrared chemical sensor using bragg wavelength in subwavelength grating structure,” *Nanomaterials (Basel)* **8**(11), 893 (2018).
 50. N. Chen, B. Dong, X. Luo, H. Wang, N. Singh, G.-Q. Lo, and C. Lee, “Efficient and broadband subwavelength grating coupler for 3.7 μm mid-infrared silicon photonics integration,” *Opt. Express* **26**(20), 26242–26256

- (2018).
51. J. Wei, F. Sun, B. Dong, Y. Ma, Y. Chang, H. Tian, and C. Lee, "Deterministic aperiodic photonic crystal nanobeam supporting adjustable multiple mode-matched resonances," *Opt. Lett.* **43**(21), 5407–5410 (2018).
 52. Y. Ma, B. Dong, B. Li, K.-W. Ang, and C. Lee, "Dispersion engineering and thermo-optic tuning in mid-infrared photonic crystal slow light waveguides on silicon-on-insulator," *Opt. Lett.* **43**(22), 5504–5507 (2018).
 53. Y. Ma, B. Dong, B. Li, J. Wei, Y. Chang, C. P. Ho, and C. Lee, "Mid-infrared slow light engineering and tuning in 1-D grating waveguide," *IEEE J. Sel. Top. Quantum Electron.* **24**(6), 6101608 (2018).
 54. Y. Chang, D. Hasan, B. Dong, J. Wei, Y. Ma, G. Zhou, K. W. Ang, and C. Lee, "All-dielectric surface-enhanced infrared absorption-based gas sensor using guided resonance," *ACS Appl. Mater. Interfaces* **10**(44), 38272–38279 (2018).
 55. W. D. Sacher, Y. Huang, G. Lo, and J. K. S. Poon, "Multilayer silicon nitride-on-silicon integrated photonic platforms and devices," *J. Lit. Technol.* **33**(4), 901–910 (2015).
 56. C. Chen, D. A. Mohr, H.-K. Choi, D. Yoo, M. Li, and S.-H. Oh, "Waveguide-integrated compact plasmonic resonators for on-chip mid-infrared laser spectroscopy," *Nano Lett.* **18**(12), 7601–7608 (2018).
 57. Y. Luo, M. Chamanzar, A. Apuzzo, R. Salas-Montiel, K. N. Nguyen, S. Blaize, and A. Adibi, "On-chip hybrid photonic-plasmonic light concentrator for nanofocusing in an integrated silicon photonics platform," *Nano Lett.* **15**(2), 849–856 (2015).
 58. M. Février, P. Gogol, A. Aassime, R. Mégy, C. Delacour, A. Chelnokov, A. Apuzzo, S. Blaize, J. M. Lourtioz, and B. Dagens, "Giant coupling effect between metal nanoparticle chain and optical waveguide," *Nano Lett.* **12**(2), 1032–1037 (2012).